Templating of Gold Nanocrystals in Micellar Cores of Block Copolymer Films

Luciana Meli,[†,§] Yuan Li,[‡] Kwon Teak Lim,[||] Keith P. Johnston,[†] and Peter F. Green*[,§]

Department of Chemical Engineering, Graduate Program in Materials Science and Engineering, The University of Texas at Austin, Austin, Texas 78712; Division of Image and Information Engineering, Pukyong National University, Pusan 608-739, South Korea; and Department of Materials Science and Engineering, The University of Michigan, Ann Arbor, Michigan 48109

Received April 8, 2007; Revised Manuscript Received June 22, 2007

ABSTRACT: Thin film functional hybrid materials composed of inorganic nanocrystals sequestered within a self-assembled template are important for a diverse range of applications, from sensors to device electronics. The properties of these materials can be "tailored" by control of composition over various length scales; the major processing challenges are associated with understanding and controlling external factors, such as confinement and interfacial interactions, that affect the self-organization process. Spin-cast polystyrene-*b*-poly(1,1′,2,2′-tetrahydroperflurooctyl methacrylate) (PS-*b*-PFOMA) diblock copolymer films can form a micellar structure, with a PFOMA core (PS corona), and are induced to undergo a transition by annealing in supercritical CO_2; consequently, the PS segments form the core with a PFOMA corona. We show that functionalized Au nanocrystals, initially dispersed within the corona (the PS phase) of the micelles, follow the morphological inversion and become sequestered within the core, now composed of PS chains; the nanoparticles segregate primarily at the PS/PFOMA interface within the core. These inversion experiments were performed on nanocomposite films with thicknesses $h \leq 150$ nm. Therefore, only one or two layers of micelles spanned the entire film. The nanoparticles were not distributed uniformly throughout the films but remained primarily near the substrate. Several competing factors determine the overall distribution of nanoparticles: the van der Waals interaction between nanoparticles and interfaces, favorable ligand−block enthalpic interactions, and the conformational entropy of the host chains.

1. Introduction

The development of strategies to tailor and to control the structure of block copolymers (BCP) containing nanocrystals, block copolymer nanocomposites, is an especially active area of research. The in-situ synthesis of the nanocrystals within the ordered domains, as a route to incorporate the nanoparticles within the BCP, is a common strategy.[1−7] One drawback of this approach is that control of the size, shape, and ordering of the nanoparticles is limited. An alternate approach is the so-called co-assembly strategy,[8−11] wherein the nanocrystals are first synthesized, enabling control of their size and shape, and subsequently compatibilized with either of the constituent blocks. With this strategy, the nanocrystals are incorporated within one phase, for example, spherical micelle cores. If the particles are to occupy the continuous phase, a new copolymer would have to be synthesized. Alternatively, the structure could be manipulated with the addition of homopolymer chains to promote a transition from one phase to an adjacent phase in the phase diagram.

Changes in the structure of the nanocomposite can also be achieved by modifying the size[12] and the surface chemistry of nanoparticles[13] during their synthesis. Generally, it has been observed that relatively small particles which are selective to one of the blocks will be reasonably well distributed throughout that domain (with some enrichment near the block interface) to maximize their translational entropy. As the particle size is increased, the stretching energy of the BCP chains increases. Thus, larger particles will segregate to the center of that block domain to reduce chain stretching.[12,14] Particles with neutral interactions for both blocks will locate preferentially at the block interface, effectively screening repulsive interactions between the blocks and consequently minimizing the overall energy of the system.[13,15,16]

One strategy that does not involve changing the composition of the copolymer or the nanocomposite is to induce a morphological transition via thermal or solvent treatment. To our knowledge, the possibility of changing the location of nanoparticles through a temperature-induced or a selective solvent-induced phase transition has not been realized to date.

In this paper, we demonstrate that it is possible to obtain a nanostructured BCP nanocomposite thin film with a switchable spatial distribution of embedded nanoparticles between the core and the corona. Specifically, PS-*b*-PFOMA copolymers form a micellar film when spin-cast from a toluene/freon cosolvent onto a silicon nitride substrate. The PFOMA component forms the cores and the PS chains (coronae) form the continuous phase of the film. PS-capped gold nanocrystals are incorporated only within the continuous phase when a solution containing the copolymer, gold nanocrystals, and the cosolvent is spin-cast on the substrate. Upon annealing in supercritical carbon dioxide, ($scCO_2$), the structure inverts and the PS chains subsequently constitute the core, now harboring the nanocrystals closer to the block interface, with the PFOMA chains forming a continuous (corona) phase. This procedure allows us to template single dispersed micellar cores of the BCP film containing gold nanocrystal domains. Moreover, an analysis of the distribution of gold nanoparticles across the films demonstrates that the

* Corresponding author. E-mail: pfgreen@umich.edu.
[†] Department of Chemical Engineering, The University of Texas at Austin.
[‡] Graduate Program in Materials Science and Engineering, The University of Texas at Austin.
[§] The University of Michigan.
[||] Pukyong National University.

10.1021/ma0708287 CCC: $37.00
Published on Web 08/04/2007

nanoparticles enrich the substrate region. These results shed some light onto the energetic interactions that control the formation of nanostructures within them and thus highlight important issues pertinent to the fabrication of thin film composite materials with hierarchically ordered nanoparticle arrays.

2. Experimental Section

2.1. Sample Preparation. The block copolymer studied in this work is an asymmetric polystyrene-*b*-poly(1,1′,2,2′-tetrahydroperfluorooctyl methacrylate) (PS-*b*-PFOMA), with a M_{nPS}/M_{nPFOMA} = 27 000/127 000, as determined by H NMR. The details of the synthesis performed by Lim and co-workers have been reported elsewhere.[17]

The PS-*b*-PFOMA diblock was dissolved in an 80:20 wt % mixture of 1,1,2-trichlorotrifluoroethane (Freon 113) (Aldrich) and toluene (Fisher Scientific) to yield clear solutions with a polymer concentration of 0.5−2 wt %. Additional solutions containing presynthesized gold nanoparticles stabilized with thiol-terminated polystyrene ligands (PSSH) (M_n = 1000 g/mol from Polymer Source Inc.) were prepared. The Au nanocrystals were synthesized by a modification of the two-phase arrested precipitation method reported by Brust et al.[18] using a 1/5 PSSH/$HAuCl_4$ ratio. The Au cores exhibited a relatively narrow size distribution with an average diameter of 4.9 ± 0.5 nm, as determined by scanning transmission electron microscopy (STEM). The weight fraction of nanoparticles in the diblock copolymer ranged from 5 to 10% w/w.

Films with thicknesses between 20 and 250 nm were prepared by spin-coating both the composite and the pure BCP solutions onto glass slides. After spin-coating, the films were floated on water and off the glass substrate and deposited onto transparent silicon nitride windows (SPI supplies) to achieve film uniformity. Once prepared, the films were evacuated for a period of 12 h to remove excess solvent.

Supercritical CO_2 annealing was performed by loading the samples into a fixed volume cell, which was subsequently sealed and pressurized with carbon dioxide (Air Products, >99.999%) using a manual pressure generator (High-Pressure Equipment Co.) and heated to the desired temperature in a water bath. The pressure was controlled with a strain gauge pressure transducer (Sensotec) calibrated to within $\pm 7 \times 10^{-3}$ MPa. We note that at the conditions studied, 75 °C and a pressure of 13.8 MPa, both of the blocks are in a plasticized state.[19−21] After a period of 72 h, the cell was cooled to room temperature and depressurized by venting CO_2 as a vapor from the top of the cell.

For cross-sectional imaging of as-cast and CO_2 annealed samples, the nanocomposite films were spin-coated directly on silicon substrates with a silicon nitride layer of 100 nm grown by LPCVD (WaferNet, Inc.). Following deposition, the films were exposed to plasma treatment for a few seconds to ionize the surface and thus enhance adhesion with the carbon layer that was subsequently evaporated on top of the film for protection. An epoxy resin layer (SPI-Pon 812, purchased from SPI supplies) was then deposited and cured on top of the carbon-covered surface, and separation of the film from the silicon nitride substrate was then realized by exposing the sample to liquid nitrogen. The uncovered interface was again layered with carbon and epoxy resin, forming a sandwiched structure that was sectioned into 100 nm thick samples using ultramicrotomy. Microtoming was performed at room temperature in a Reichert Ultracut-E ultramicrotome using a diamond knife.

2.2. Sample Characterization. Characterization of the films was achieved by a combination of scanning force microscopy and scanning transmission electron microscopy. Ex-situ images of the topography of the films were taken with Nanoscope IV and Nanoscope IIIa (Digital Instruments) scanning force microscopes operating in tapping mode.

The morphology of the diblock copolymer films, as well as the distribution of the nanoparticles within them, was analyzed with a JEOL 2010F transmission electron microscope operating at an accelerating voltage 200 kV in scanning mode (STEM) using a high-angle annular dark field (HAADF) detector. HAADF imaging, also called Z-contrast imaging, allows observation of the species present based on differences in atomic number, density, and sample thickness. Thus, in our pure copolymer films, contrast in the image is given by the difference in densities of the two constituent blocks, having the denser PFOMA regions ($\rho_{20°C}$ = 1.53 g/mL) appear brighter than the PS domains ($\rho_{20°C}$ = 1.06 g/mL). In some instances, samples were exposed to the vapor of an aqueous RuO_4 solution (SPI supplies) for 5 min to selectively stain the PS-rich domains. In this case, the selectively adsorbed ruthenium compound gives a higher intensity to the PS phase, since contrast in this technique is particularly sensitive to the atomic number of the species present.

Dynamic secondary ion mass spectrometry (DSIMS) was used to obtain the depth profile of Au within the block copolymer films. The films were spin-coated directly on the silicon nitride substrates described above. Prior to the analysis, the thickness of the films was measured using spectroscopic ellipsometry (J.A. Wollam Co., Inc.). SIMS was performed at UCSB with a Physical Electronics 6650 quadropole secondary ion microscope. Sputtering was accomplished with the use of a cesium primary ion beam monitoring negative secondary ions. The negative carbon and silicon secondary ion currents were measured to monitor the stability of the profile and to serve as indicators of the polymer−air and polymer−substrate interfaces. These profiles, along with the previously determined film thickness, allowed us to convert the sputtering time to a depth scale. Since in these studies we are not concerned about the absolute Au concentration, the Au^- signal was scaled to yield a maximum value of 1 and a minimum value of 0.

3. Results and Discussion

This article is organized as follows. The micellar structure of the PS-*b*-PFOMA diblock copolymer spin-coated from a freon/toluene solution, as well as the phase inversion of the core−shell morphology induced by $scCO_2$ annealing, is first described. Results for the sequestering of gold particles within the PS phase are then examined, followed by a discussion of the structural inversion. Two related observations are discussed: (1) the shape of the micellar structures that develop in the films after $scCO_2$ processing and (2) the influence of the proximity of interfaces on the depth distribution of nanoparticles within the film.

3.1. Micelle-like Aggregate Formation and Phase Inversion of Neat PS-*b*-PFOMA Diblock Copolymer. The structure of the as-cast PS-*b*-PFOMA copolymer films produced using a toluene/freon cosolvent solution is now described. The images in Figure 1 indicate that PS-*b*-PFOMA forms micellar aggregates after spin-casting; PFOMA cores of roughly 50 nm in diameter are embedded in a continuous PS (corona) matrix (see diagram in Figure 1a). The spherical topography is evident from the SFM image of a h = 22 nm thick film, shown in Figure 1b. The PS component of the film was selectively stained with ruthenium tetroxide (RuO_4) to yield greater contrast and imaged using STEM to obtain the Z-contrast images shown in part c. The PS component is represented by the bright regions, while the circular PFOMA cores are represented by the darker regions. Z-contrast images of a thicker (h = 72 nm) as-cast PS-*b*-PFOMA film demonstrate the appearance of overlapping circular features, which are indicative of the presence of two layers of micellar aggregates across the film thickness (Figure 1d). The formation of the PFOMA-core micelles, discussed in further detail in ref 12, occurs during the spin-coating process and is a consequence of the faster evaporation rates of Freon 113 relative to toluene, in which the PS chains are more soluble. It is important to emphasize that rapid aggregate formation caused by the solvent evaporation during spin-coating, as well as

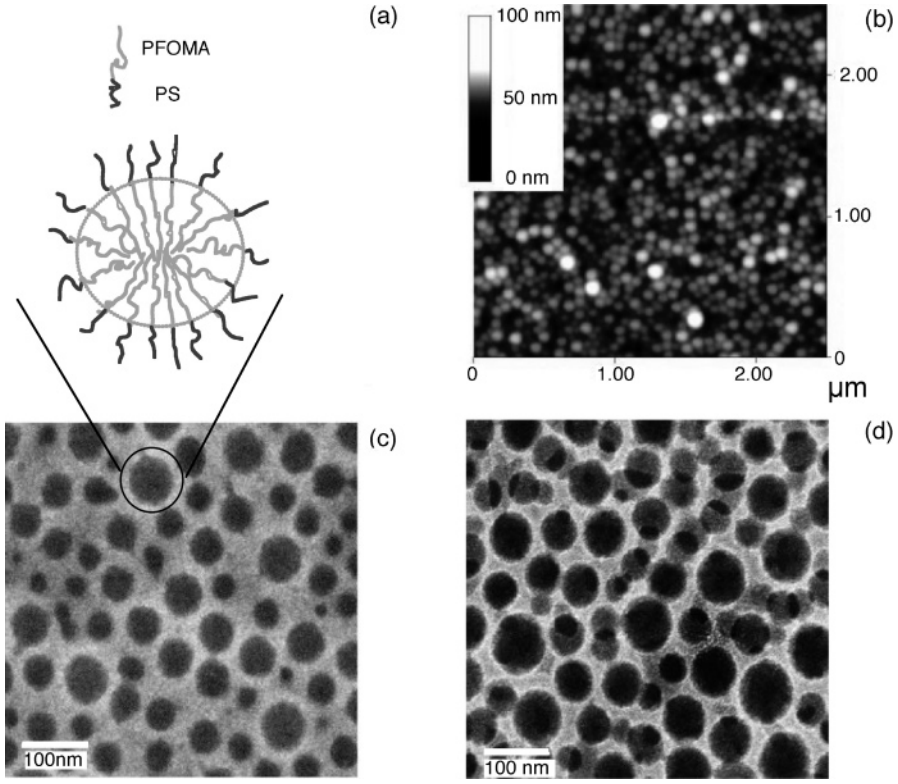

Figure 1. Morphology of an as-cast PS-*b*-PFOMA film on a silicon nitride substrate: (a) Schematic diagram of aggregate morphology. (b) SFM image of the micellar aggregates in a 22 nm thick film; the average diameter of the micelles (core plus corona) is 80 nm. (c) Corresponding STEM−HAADF image of the stained film with an average PFOMA core diameter of 50 nm. (d) Z-contrast image of a stained 72 nm film presenting two layers of micellar aggregates.

variations in solvent quality due to the faster evaporation rate of freon, is likely to yield a nonequilibrium morphology in these films. Evidence of the nonequilibrium nature of the morphology is obtained from the relatively broad distribution of aggregate core size ($\sigma/\langle D\rangle = 0.21$), which is typically narrow for block copolymer micelles. It is also possible that the formation of transient morphologies is promoted by the existence of a very strong interfacial tension between blocks, not unexpected for a BCP with a fluorinated block characterized by an extremely low cohesive energy density.[22] Another factor that may contribute to this is the large asymmetry of the BCP ($f_{PFOMA} = 0.75$), which favors aggregates with PS cores.

Upon annealing the diblock in $scCO_2$, which is highly selective toward the fluorinated block,[17] the structure inverts and the PS chains now constitute the core of the micelles. An SFM scan of a 240 nm thick PS-*b*-PFOMA film annealed at 75 °C, and a CO_2 pressure of 13.8 MPa, reveals the presence of micelles, much like those observed for the as-cast films (Figure 2a). The Z-contrast image of the stained film (Figure 2b) indicates that the structure of the aggregates has completely inverted in the $scCO_2$ environment to form PS cores with a surrounding PFOMA shell, as depicted in the diagram of Figure 2c. The image in Figure 2b also shows the existence of several layers of micelles in this thick film; on the other hand, a single layer of aggregates comprises the thinner $h = 70$ nm film of Figure 2d. This phase transformation opens up the possibility of controlling micelle formation and morphology by adjusting the solvent quality through manipulation of pressure and/or temperature of the system. Indeed, detailed studies on this system demonstrate that it is also possible to tune micellar size through careful adjustments of the CO_2 density.[17]

We note, for the moment, that confinement of these micellar aggregates to a thin film geometry is expected to have an influence on the shape of the aggregates. For example, it is evident that the core to film thickness ratio of the as-cast sample in Figure 1b,c demonstrates that the aggregates in this film cannot be spherical in shape and are likely to develop an ellipsoidal shape. We will discuss in more detail the effects of interfaces and confinement on the structure of the aggregates with PS cores in section 3.3.

3.2. Phase Inversion of Sequestered Gold Nanocrystals. The strategy for coassembly of diblock copolymers and nanoparticles relies on tailoring the surface chemistry of the nanocrystal such that it exhibits a stronger affinity for one block.[23] In our case, we compatibilized Au nanoparticles with thiol-terminated, low molecular weight polystyrene, thereby rendering the nanocrystal−PS system to interact favorably with the PS domains. In these experiments, the film thickness was chosen such that only one or two layers of micelles spanned the entire film. A Z-contrast image of an unstained, as-cast 70 nm thick film containing 10% w/w of Au−PS_{10}SH reveals (Figure 3a) that the nanoparticles are indeed preferentially located within the continuous PS phase. (For this unstained film, the higher density PFOMA core domains appear bright.) This film is sufficiently thick to be composed of two layers of micelles. However, we observe that without RuO_4 staining the contrast between PS and PFOMA is only strong enough to show one layer of micellar aggregates. The staining of a similar film allows us to image micelles in different layers, as shown in Figure 3b.

In Figure 4, the morphology of a PS-*b*-PFOMA/Au−PS_{10}-SH nanocomposite film (5% w/w) annealed in CO_2, at 75 °C and 13.8 MPa is presented. From the Z-contrast image it is evident that the inversion of the as-cast morphology has been achieved, and the nanocrystals are constrained to follow the morphological change; i.e., they form nanostructures that mimic

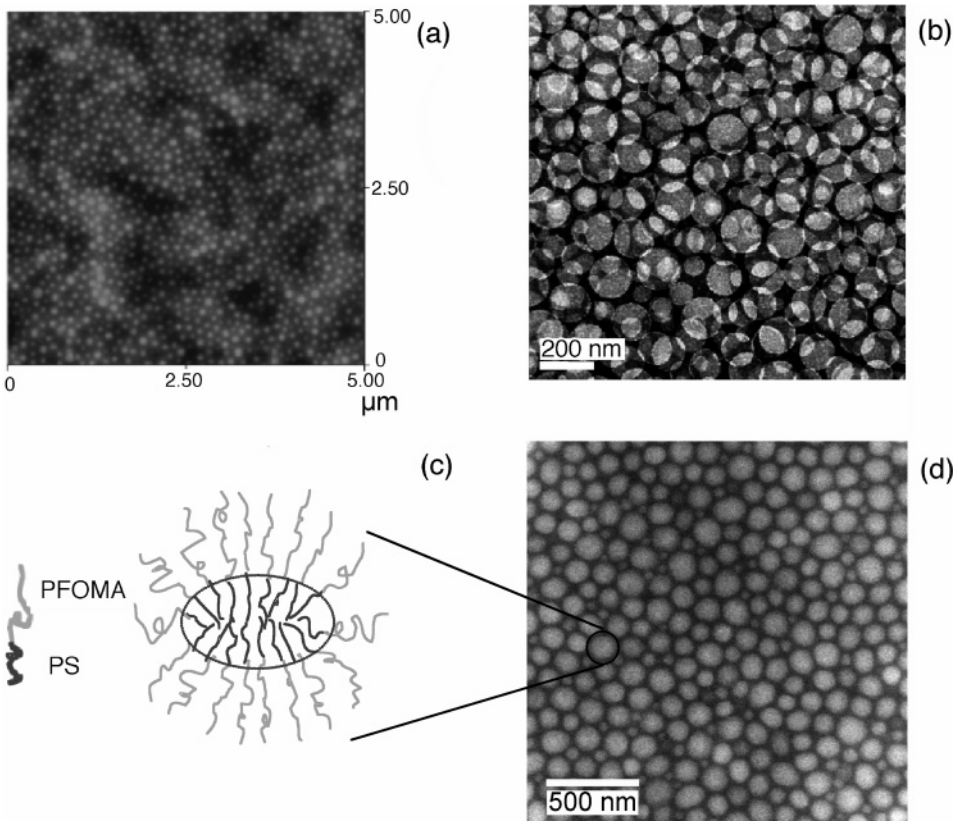

Figure 2. Morphology of a PS-*b*-PFOMA film after $scCO_2$ processing at 75 °C and 13.8 MPa. (a) SFM image of a 240 nm thick film annealed for a period of 72 h. (b) STEM−HAADF image of the same film stained with RuO_4, depicting the presence of several micellar layers. (c) Schematic drawing of the aggregate structure showing the inversion of the microdomains into PS cores. (d) STEM−HAADF image of a 70 nm thick film stained with RuO_4 and presenting a single layer of micelles; the film was processed in $scCO_2$ for 10 days.

the morphology of the dispersed PS phase. The PS core domains in this 64 nm thick film have an average characteristic size of 97 nm with a broad distribution of sizes (ranging from 35 to 160 nm) and contain ~20 nanoparticles per aggregate.

3.3. Shape of PS-*b*-PFOMA Micellar Aggregates Annealed in $scCO_2$. The feasibility of switching the location of nanocrystals in conjunction with the block copolymer template has been established, and we now direct our attention to the size and shape of the micellar structures, focusing on the CO_2 annealed films. A cross-sectional, Z-contrast image of a PS−PFOMA nanocomposite film containing 10% w/w of Au−PS_{10}-SH annealed in $scCO_2$ shows that aggregates closest to the free surface tend to adopt an ellipsoidal configuration (Figure 5a), with the major axis lying parallel to substrate ($B/A = 1.24$, where B and A are the major and minor axis defined in the schematic representation of Figure 5c). Eisenberg and co-workers[24] have estimated the size of a typical block copolymer micelle in solution from the degree of core-chain stretching, S_c, specified by $S_c = R/l_e$, where R is the radius of the micelle core and l_e is the end-to-end distance of the PS block in the unperturbed state ($l_{e-PS} = 10.5$ nm).[24] As mentioned in ref 12, values of S_c found in the literature range from 0.7 to 1.5. In our case, R is equal to the minor axis, A, measured from the cross-section image of the nanocomposite film ($\langle A \rangle = 23.1$ nm). The data show that the degree of stretching of the core PS block is high in comparison to other systems reported in the literature ($S_c = 2.2$). The high degree of stretching may be explained by considering that the PS block can swell up to 22% with RuO_4, as measured by Sohn and co-workers[7] for a PS−PMMA diblock copolymer. Other factors that may help explain this discrepancy are the possible deformation of the aggregates during microtomy[25] as well as effect of confinement and interfacial interactions in the degree of stretching of the block copolymer chains.[26,27]

It is worth mentioning that the cross-sectional image of this film also reveals the fact that these ellipsoidal aggregates do not contain gold nanocrystals within them. We will return to this point later, when the data in Figure 6, showing a depth profile of the nanoparticles, are discussed.

Up to now, we have examined the size and shape of the micelle-like aggregates near the free surface, but we have failed to mention that aggregates closest to the substrate seem to be forming spherical caps, with a base radius, L (see Figure 5c), significantly larger than the major axis of the ellipsoidal aggregates above them ($\langle L \rangle = 76.2$ nm, while $\langle B \rangle = 28.6$ nm). These spherical-capped aggregates could be easily mistaken for surface micelles that have the core block directly adsorbed to the substrate.[28,29] However, measurements of the average height of the aggregates, $\langle h \rangle$, show that a PS core chain would have to be stretched nearly 6 times its unperturbed dimensions if indeed the height of the core was approximately the length of one PS block chain ($\langle h \rangle = 59.1$ nm). This leads us to believe that the height of the spherical-capped core is composed of two PS block chains, as depicted in the schematic of Figure 5c. The internal structure described above would allow for a more realistic degree of core chain stretching ($S_c = \langle h \rangle / 2l_e = 2.7$), especially if one considers that in this case the core is swollen not only by the staining agent but also by the gold nanoparticles sequestered within it. Such a structure would also allow the adsorption of the PFOMA block onto the substrate, assuming there is a preferential affinity between the carbonyl groups in the PFOMA monomer and the polar silicon nitride substrate. However, this cannot be corroborated from the cross-sectional image since we cannot

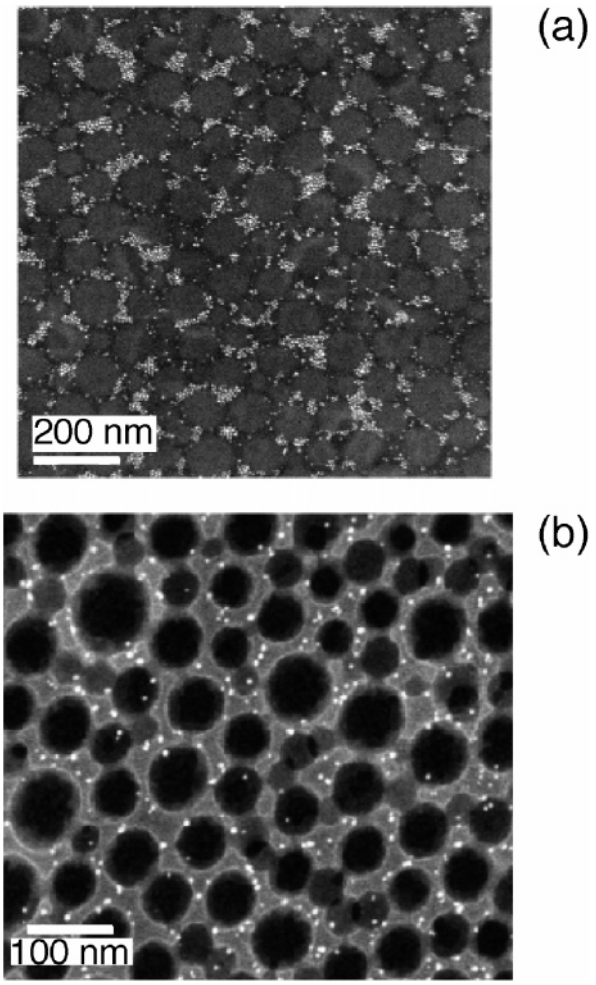

Figure 3. Internal structure of an as-cast PS-*b*-PFOMA film loaded with Au−PSSH nanoparticles. (a) STEM−HAADF image of a 70 nm thick film showing the sequestering of the Au nanoparticles to the PS coronae (10% w/w). This film is not stained, and consequently the higher density, PFOMA block appears brighter than the PS corona phase. (b) STEM−HAADF image of a 60 nm thick film stained with RuO_4 (5% w/w).

differentiate between the PFOMA block and the epoxy resin in which the BCP is embedded.

It is important to mention that the existence of the two types of micellar aggregates shown in the cross section of the BCP film, the spherical-capped aggregates and the ellipsoidal aggregates, each with a characteristic size, explains to some extent the broad distribution of sizes measured in the in-plane image of the film (Figure 4).

The distortion in the shape of the micelles is likely to be the result of the preferential interactions between the PFOMA block and the substrate. That is, the strong affinity between the PFOMA chains and the polar silicon nitride substrate may cause the PFOMA chains to be somewhat anchored on the substrate, leading to a deformation of the curvature of the micelles close to this interface. The chains located next to the substrate will therefore form a planar interface (brush), while an undulation will develop in the chains directly above them to match onto the ellipsoidal shape of the aggregates in the subsequent layer, and eventually form a bulk spherical phase when the film is thick enough.

Another possible explanation for the distortion in the shape of the micelles is the formation of nonconventional morphologies due to a strong interfacial tension between blocks, anticipated by superstrong segregation theory (SSST).[30,31] The theory predicts the transition from spherical micelles to oblate ellipsoids to disklike micelles and finally to flat sheets as the interfacial tension between blocks increases. More recently, Lodge and co-workers used this theory to explain the formation of flat disk micelles by self-assembly of a fluorinated diblock copolymer in an organic solvent.[32] It is thus possible that the extremely low cohesive energy density of the PFOMA leads to a strong repulsive interaction between blocks, which in turn can cause deviations from sphericity in the aggregates. Furthermore, it is possible that the already large repulsive interaction between blocks may be enhanced by both the presence of a selective solvent and the presence of the substrate (which has been show to enhance segregation in other BCP/$scCO_2$ thin film systems).[33]

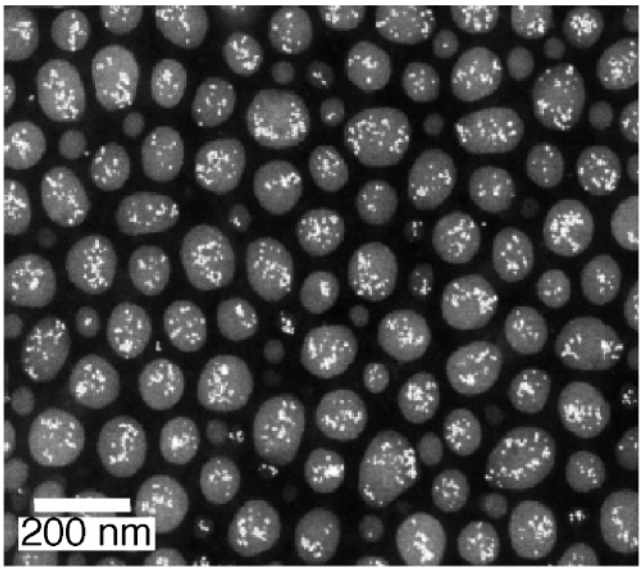

Figure 4. STEM−HAADF image of a single-layered, 64 nm PS-*b*-PFOMA film with 5% w/w nanoparticle loading; the film was processed for 15 days in $scCO_2$ (T = 75 °C and P = 13.8 MPa). The image clearly shows that the Au nanoparticles are able to follow the morphological transition induced by $scCO_2$.

3.4. Depth Distribution of Gold Nanoparticles across PS-*b*-PFOMA Films. Cross-sectional images of the as-cast, as well as the CO_2-annealed BCP/nanocomposite films, are shown in parts a and b of Figure 5, respectively. In both films, the gold nanoparticles seem to be segregated to the substrate. To obtain more information on the Au particle distribution across the films, we monitored the secondary ion count rate of C, Si, and Au negative ions as a function of sputtering time using dynamic secondary ion mass spectroscopy (DSIMS). The Au signal from an as-cast, 160 nm PS-*b*-PFOMA/Au−PSSH thick film (5% w/w) was normalized to yield the relative concentration profile shown in Figure 6a. The presence of a Gaussian peak near the silicon nitride substrate after normalization is evident. Thus, the SIMS analysis confirms that the gold particles are preferentially segregated to the substrate (Figure 5d) spanning a region no thicker than 30 nm, obtained from the full width at half-maximum (fwhm). The depth profile of Au in a 108 nm thick PS-*b*-PFOMA film (5% w/w) annealed in CO_2 was subsequently obtained (Figure 6b), verifying that there is still considerable enrichment of Au near the substrate after CO_2 processing, for the thickness and concentration analyzed.

Computational studies on filled BCP systems confined between two identical surfaces have shown that the polymer melt can induce an entropic depletion attraction between the nanoparticles and walls, whereby a fraction of particles is driven to the interfaces to increase the conformational entropy of the BCP chains.[34] In our experiments, the interfacial interaction

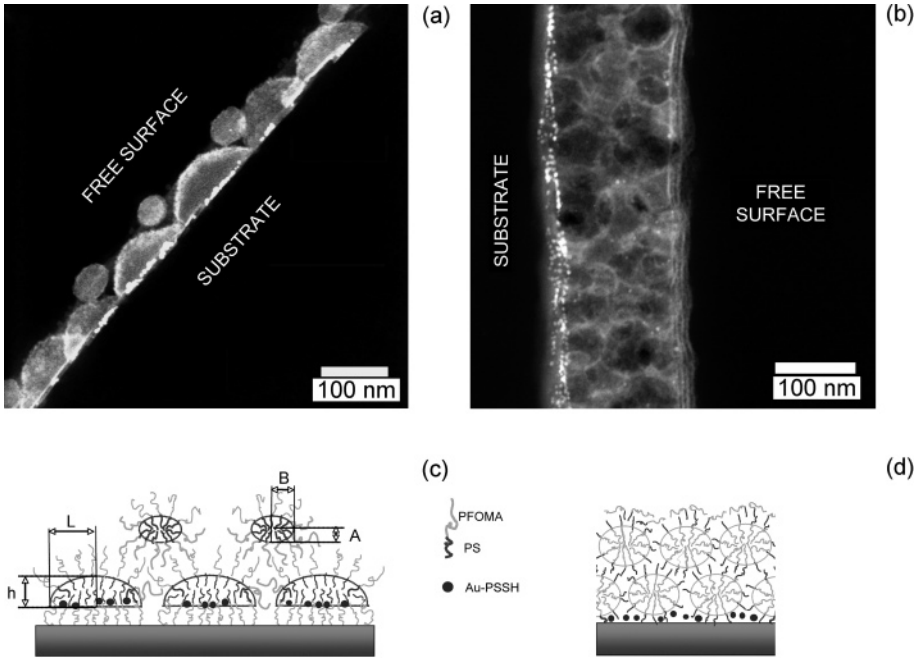

Figure 5. (a) Cross-sectional STEM-HAADF image of a PS-*b*-PFOMA film with 5% w/w nanoparticle loading after $scCO_2$ processing (T = 75 °C, 13.8 MPa, and t = 15 days). **(**b**)** Cross-sectional, STEM−HAADF image of an as-cast PS-PFOMA film with Au−PSSH (5% w/w). **(**c**)** Schematic diagram of the internal structure of the film shown in (a), depicting the formation of ellipsoidal aggregates close to the free surface and spherical-capped aggregates near the substrate, where the nanoparticles are selectively segregated. **(**d**)** Schematic representation of the structure of the as-cast film shown in (b) illustrating the preferential segregation of the Au−PSSH particles to the substrate. All of the samples in this figure were stained with RuO_4 prior to imaging. Note that the schematic diagrams in (c) and (d) differ slightly from the morphology proposed by Li et al.,[17] particularly in the proximity of the substrate. This slight modification does not change the validity of the analysis proposed in this reference.

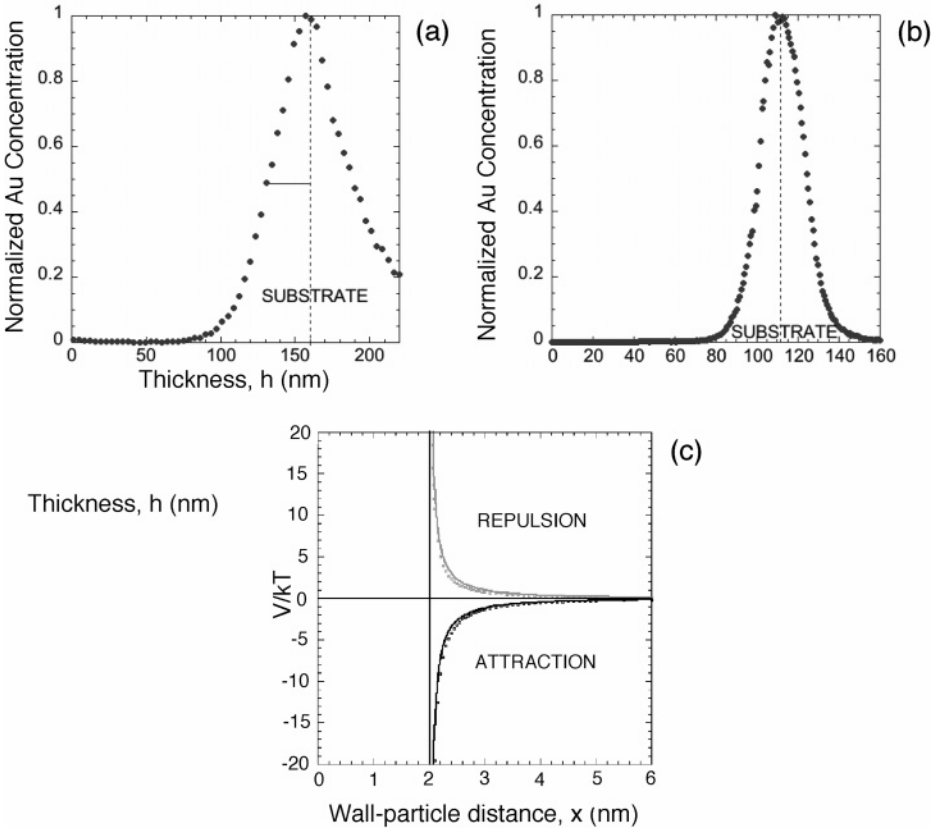

Figure 6. (a) DSIMS concentration profile showing enrichment of Au near the substrate for an as-cast, 160 nm thick film containing 5% w/w of nanoparticles. **(**b**)** DSIMS Au concentration profile of a 108 nm thick film (5% w/w) annealed in $scCO_2$ at 75 °C and 13.8 MPa, demonstrating that preferential segregation of Au to the substrate is still prevalent. **(**c**)** Calculated van der Waals interaction between a sheathed Au sphere and a wall; the gray curves show a net repulsion between the particles and the free surface, while the black curves show a net attraction between the Au cores and the silicon nitride substrate. Circles (●) correspond to $scCO_2$ environments, and solid lines represent the same calculation under air.

between the gold nanoparticles and the interfaces, free surface and substrate, should not be symmetric. Considering that both Au and silicon nitride are high-energy surfaces, it is likely that the PS brush covering the particles may not be sufficiently thick

to adequately screen the attractive interactions between substrate and gold and thus lead to preferential segregation of the gold nanoparticles to this interface.

We explored this possibility by estimating the nonretarded, long-range, van der Waals interactions between a sheathed sphere and a wall, following a microscopic approach for multilayer structures.[35] We considered that the intervening polymeric medium was composed of a 25:75 mixture of PS and PFOMA, respectively, while the adsorbed $PS_{10}SH$ layer was assumed to be an impenetrable PS layer of 2 nm in thickness. The details of this calculation are included as Supporting Information. As expected, the effective interface potential between the sheathed Au particle and the silicon nitride substrate, depicted in Figure 6c, shows a net attraction between the crystals and the macroscopic body. On the other hand, a repulsive force between these particles and the free surface is obtained when substituting the silicon nitride wall for air. Qualitatively, the same result is obtained when the interfacial energy calculation accounts for the presence of CO_2, as a pure phase as well as adsorbed within the polymer film and in the ligand (Figure 6c). Therefore, the rough interaction energy calculations are consistent with our experimental observations of preferential segregation of gold toward the substrate.

It is important to emphasize that the proposed internal morphology of the $scCO_2$ annealed film implies that the gold nanoparticles are actually located at the interface between the PS and the PFOMA block in the spherical-capped aggregates, as illustrated in Figure 5c. This result is unexpected, considering that the size of the gold nanoparticles is comparable to the radius of gyration of the BCP chain ($D \approx R_{g,PS-PFOMA}$, where D is the diameter of the nanoparticle considering a brush thickness of ~1.9 nm). Theoretical and experimental studies would then suggest that these relatively large particles should be segregated to the center of the PS microdomains,[14,36] where the loss in conformational entropy of the chains is minimized. Our results suggest that the chain entropy loss incurred by allocating the particles at the block interface is overcome by the enthalpic gain of bringing them closer to the substrate. An additional factor that may need to be evaluated when considering the location of the nanoparticle is the width of the interface between the neighboring blocks.[37]

4. Conclusions

Our findings demonstrate the feasibility of using selective solvent annealing as a means of controlling composite nanostructure in a dynamic fashion. While the phase inversions that enable control of the nanocomposite structure can be accomplished by exposing a BCP to any selective solvent, the use of supercritical fluids offers the possibility of tuning the morphology of the polymer in a very controlled manner. This follows from the fact that the solvent quality can be easily adjusted with pressure and temperature. Indeed, in a previous publication[17] we demonstrated that the size of the micellar PS core in this PS−PFOMA diblock copolymer can be gradually increased by increasing the $scCO_2$ annealing temperature. Moreover, plasticization of the film and supercritical fluid absorption may also enhance diffusion of the nanoscopic particles in comparison to liquid solvents, facilitating the templating of the nanoparticles within the BCP.

Finally, we note that there are a number of studies that have focused on understanding how to control the distribution of nanoparticles within a bulk BCP by manipulating nanoparticle−polymer interactions. In this work, apart from exploiting the inversion to control the location and distribution of nanoparticles, we also showed that particle−interface (free surface and substrate) interactions need to be considered for precise control of morphology in thin film composite nanostructures.

Acknowledgment. This material is based upon work supported by the STC Program of the National Science Foundation under Agreement CHE-9876674 and by DMR0601890. We thank the Center for Nano- and Molecular Science and Technology at UT-Austin, the Electron Microbeam Analysis Laboratory and the Microscopy and Image Analysis Laboratory at the University of Michigan for TEM, SFM, and ultramicrotome instruments as well as the Welch Foundation and SPRING for partial financial support of these instruments.

Supporting Information Available: Calculations of the nonretarded, long-range van der Waals interaction between a sheathed sphere and a wall. This material is available free of charge via Internet at http://pubs.acs.org.

References and Notes

(1) Abes, S. I.; Cohen, R. E.; Ross, C. A. *Chem. Mater.* **2003**, *15*, 1125−1131.
(2) Brown, G. D.; Watkins, J. J. *Polym. Mater. Sci. Eng.* **2001**, *84*, 130.
(3) Sohn, B. H.; Seo, B. H. *Chem. Mater.* **2001**, *13*, 1752−1757.
(4) Sohn, B. H.; Yoo, S. I.; Seo, B. W.; Yun, S. H.; Park, S. M. *J. Am. Chem. Soc.* **2001**, *123*, 12734−12735.
(5) Mayer, A. B. R.; Mark, J. E. *Colloid Polym. Sci.* **1997**, *275*, 333.
(6) Sohn, B. H.; Cohen, R. E. *Chem. Mater.* **1997**, *9*, 264.
(7) Park, S. M.; Yun, S. H.; Sohn, B. H. *Macromol. Chem. Phys.* **2002**, *203* (14), 2069−2074.
(8) Bockstaller, M. E.; Kolb, R.; Thomas, E. L. *Adv. Mater.* **2001**, *13*, 1783−1786.
(9) Kim, B. J.; Chiu, J. J.; Yi, G. R.; Pine, D. J.; Kramer, E. J. *Adv. Mater.* **2005**, *17*, 2618.
(10) Lauter-Pasyuk, V.; Lauter, H. J.; Ausserre, D.; Gallot, Y.; Cabuil, V.; Kornilov, E. I.; Hamdoun, B. *Physica B* **1998**, *241−243*, 1092−1094.
(11) Schmaltz, B.; Brinkmann, M.; Mathis, C. *Macromolecules* **2004**, *37*, 9056−9063.
(12) Bockstaller, M. R.; Lapetnikov, Y.; Margel, S.; Thomas, E. L. *J. Am. Chem. Soc.* **2003**, *125*, 5276−5277.
(13) Chiu, J. J.; Kim, B. J.; Kramer, E. J.; Pine, D. J. *J. Am. Chem. Soc.* **2005**, *127*, 5036−5037.
(14) Thompson, R. B.; Ginzburg, V. V.; Matsen, M. W.; Balazs, A. C. *Science* **2001**, *292*, 2469−2472.
(15) Schultz, A. J.; Hall, C. K.; Genzer, J. *Macromolecules* **2005**, *38*, 3007−3016.
(16) Wang, Q.; Nealey, P. F.; de Pablo, J. J. *J. Chem. Phys.* **2003**, *118*, 11278−11285.
(17) Li, Y.; Meli, L.; Lim, K. T.; Johnston, K. P.; Green, P. F. *Macromolecules* **2006**, *39*, 7044−7054.
(18) Brust, M.; Walker, M.; Bethell, D.; Schiffrin, D. J.; Whyman, R. *J. Chem. Soc., Chem. Commun.* **1994**, 801.
(19) Condo, P. D.; Paul, D. R.; Johnston, K. P. *Macromolecules* **1994**, *27*, 365−371.
(20) Wissinger, R. G.; Paulaitis, M. E. *J. Polym. Sci., Part B: Polym. Phys.* **1991**, *29*, 631−633.
(21) Arnold, M. E.; Nagal, K.; Freeman, B. D.; Spontak, R. J.; Betts, D. E.; DeSImone, J. M. *Macromolecules* **2001**, *34*, 5611−5619.
(22) Hillmyer, M. A.; Lodge, T. P. *J. Polym. Sci., Part A: Polym. Chem.* **2002**, *40*, 1−8.
(23) Bockstaller, M. R.; Mickiewicz, R. A.; Thomas, E. L. *Adv. Mater.* **2005**, *17*, 1331−1349.
(24) Zhang, L. F.; Eisenberg, A. *J. Am. Chem. Soc.* **1996**, *118*, 3168−3181.
(25) Cameron, N. S.; Corbierre, M. K.; Eisenberg, A. *Can. J. Chem.* **1999**, *77*, 1311−1326.
(26) Milner, S. T.; Witten, T. A.; Cates, M. E. *Macromolecules* **1988**, *21*, 2610−2619.
(27) Milner, S. T. *Europhys. Lett.* **1988**, *7*, 695−699.
(28) Shull, K. R. *Macromolecules* **1993**, *26*, 2346−2360.
(29) Ligoure, C. *Macromolecules* **1991**, *24*, 2968−2972.
(30) Nyrkova, I. A.; Khokhlov, A. R.; Doi, M. *Macromolecules* **1993**, *26*, 3601−3610.
(31) Semenov, A. N.; Nyrkova, I. A.; Khokhlov, A. R. *Macromolecules* **1995**, *28*, 7491−7500.
(32) Edmonds, W. F.; Li, Z. B.; Hillmyer, M. A.; Lodge, T. P. *Macromolecules* **2006**, *39*, 4526−4530.
(33) Arceo, A.; Green, P. F. *J. Phys. Chem. B* **2005**, *109*, 6958−6962.

(34) Lee, J. Y.; Thompson, R. B.; Jasnow, D.; Balazs, A. C. *Macromolecules* **2002**, *35*, 4855−4858.
(35) Nir, S. *Prog. Surf. Sci.* **1976**, *8*, 1−58.
(36) Kim, J. U.; O'Shaughnessy, B. *Macromolecules* **2006**, *39*, 413−425.
(37) Haryono, A.; Binder, W. H. *Small* **2006**, *2*, 600−611.
(38) Meli, L.; Pham, J. Q.; Johnston, K. P.; Green, P. F. *Phys. Rev. E* **2004**, *69*, 051601-1−051601-8.
(39) Ackler, H. D.; French, R. H.; Chiang, Y. T. *J. Colloid Interface Sci.* **1996**, *179*, 460−469.
(40) Israelachvili, J. N. *Intermolecular and Surface Forces*, 2nd ed.; Academic Press: Suffolk, UK, 1992; p 450.
(41) Arnold, M. E.; Nagai, K.; Spontak, R. J.; Freeman, B. D.; Leroux, D.; Betts, D. E.; DeSimone, J. M.; DiGiano, F. A.; Stebbins, C. K.; Linton, R. W. *Macromolecules* **2002**, *35*, 3697−3707.
(42) Lewis, J. E.; Biswas, R.; Robinson, A. G.; Maroncelli, M. *J. Phys. Chem. B* **2001**, *105*, 3306−3318.

MA0708287